Cancer Nanotechnology

RESEARCH Open Access

Evaluation of the performance of Fe_3O_4/MnO_2@doxorubicin hybrid nanozymes on multicellular structure and their therapeutic management to limit the growth of human breast cancer cells

Majid Sharifi[1,2], Mohammad Kamalabadi-Farahani[2*], Amir-Abas Salmani[3] and Mahmoud Malaki[4]

*Correspondence:
Kamalabadi@shmu.ac.ir

[1] Student Research Committee, School of Medicine, Shahroud University of Medical Sciences, Shahroud, Iran
[2] Department of Tissue Engineering, School of Medicine, Shahroud University of Medical Sciences, Shahroud, Iran
[3] Applied Cell Sciences Division, Department of Hematology, Faculty of Medical Sciences, Tarbiat Modares University, Tehran, Iran
[4] Faculty of Basic Sciences, Gonbad Kavous University, Gonbad Kavous, Golestan, Iran

Abstract

Doxorubicin (DOX) is the most common treatment for breast cancer, but its effectiveness is limited by drug resistance and dose variability. Evidence suggests that nanozymes can significantly improve drug penetration and effectiveness in breast cancer treatment, owing to their stable and targeted catalytic properties. However, their varied responses and concentration-dependent toxicities present challenges. After developing pH-sensitive Fe_3O_4/MnO_2@DOX hybrid nanozymes (FMDHN) and evaluating their physicochemical and functional properties, their efficacy was investigated on MCF-7 cells using both two-dimensional and spheroid models. Our findings reveal that FMDHNs, sized 150–270 nm, inhibit MCF-7 cell growth through drug release triggered by acidity and photothermal therapy (PTT). The catalytic efficiency of FMHN in generating O_2 and ·OH further enhances cancer cell suppression. Doubling the effective concentrations of FMHN and DOX by transitioning from two-dimensional to spheroid cell structures could adversely affect normal cells, while a synergistic approach combining the DOX and FMHN effectively inhibits MCF-7 cell growth at non-toxic dose. Combining FMDHN with PTT enhances this inhibition, lowering the effective dose to 1.08 µg/mL and effectively managing toxicity. The cytotoxicity mechanism in MCF-7 spheroids shows that PTT with FMDHN significantly elevates pro-inflammatory cytokines, including TNF-α, CASP9, CASP7 and CASP3. Optimizing the concentration of pH-sensitive nanozymes based on their synergistic effects can minimize side effects and maximize their breast cancer treatment potential.

Keywords: Breast cancer, Spheroids, Nanozymes, Doxorubicin, Photothermal therapy

Graphical Abstract

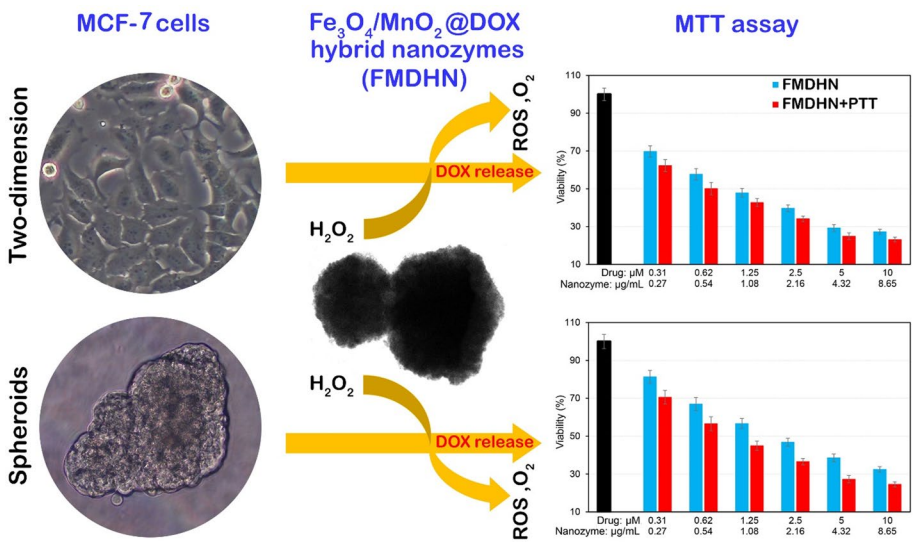

Introduction

Breast cancer is currently one of the deadliest cancers in women, with around a third of affected women dying even after mastectomy. The main treatment involves drugs, which have been very effective in improving survival rates. However, about half of patients undergoing drug therapies suffer a relapse (Wang et al. 2014). The main reason for treatment failure is resistance to anticancer drugs, caused by poor drug penetration due to significant hypoxia and blockages in tumor areas (Sharifi et al. 2022). Alongside traditional treatments like surgery, chemotherapy, and radiation therapy, nanozymes are being investigated as a less invasive option with catalytic properties (Falahati et al. 2024). In addition to their ability to targeted release of drugs in tumor environments with a pH 6.5, nanozymes exhibit promise in drug-resistant tumors treatment by increasing O_2 levels to improve drug penetration, producing radicals (O_2^- and ·OH), and synergizing with photothermal therapy (PTT) (Falahati et al. 2022; Cui et al. 2024). Among nanozymes mimicking peroxidase and catalase (Yang et al. 2022; Zhang et al. 2024), the use of Fe_3O_4 in tumor therapy is interesting due to high compatibility and Fenton reactions (Chen et al. 2019; Tang et al. 2021; Dong et al. 2022). Fe_3O_4 nanozymes are amazing for producing ·OH in acidic conditions through peroxidase-like activity on H_2O_2, as well as generating hydrogen peroxy radicals in neutral and alkaline conditions, similar to catalase-like activity for the production of O_2 and H_2O (Sun et al. 2022; Gao et al. 2007; Lei et al. 2023; Liu et al. 2022). To enhance the catalytic performance of Fe_3O_4 nanozymes, the incorporation of MnO_2 nanozymes is proposed (Zhang et al. 2021). The addition of MnO_2 not only effective in Fe^{2+} regeneration, but also reduces tumor hypoxia by converting H_2O_2 to H_2O and O_2 in acidic conditions (Chen et al. 2023a; Tang et al. 2022). Despite challenges like low selectivity and biocompatibility linked to MnO_2 (Sisakhtnezhad et al. 2023), its capacity to convert superoxide into ·OH and H_2O_2 during catalysis has increased

its potential for use in cancer therapy (Zhang et al. 2021; Chen et al. 2023a; Li et al. 2022). Furthermore, Fe_3O_4 and MnO_2 nanoparticles exhibit enhanced catalytic pathways under photothermal and photodynamic therapy activities, as evidenced in studies by Du et al. (2023), Chen et al. (2023b), Cun et al. (2022) and Zhang et al. (2021). The utilization of PTT technique to enhance thermal energy from laser irradiation in the tumor microenvironment is a non-invasive and precise method that can boost confidence in cancer treatment through synergistic interaction with nanozymes (Tang et al. 2024; Liu et al. 2024). It has been found that the heat generated by PTT enhances the glucose oxidase activity for starvation, peroxidase- and catalase-like activities of nanozymes to generate ·OH and O_2, and also restricts cancer cell growth by activating the extrinsic apoptosis pathways (Melo-Diogo et al. 2017; Lv et al. 2021; Wu et al. 2021; Chen et al. 2022a). As a result, it is anticipated that the treatment of drug-resistant tumors will be expedited through the inherent functionality of nanozymes and the cascading amplification of radicals, O_2, and heat production induced by PTT.

In addition to the significance of nanozymes and PTT in the therapeutic effects on breast cancers, the selection of the drug type is crucial. The standard treatment for advanced breast cancers involves doxorubicin (DOX), an anthracycline antibiotic (Sohail et al. 2021). DOX disrupts DNA and RNA centers, offering a reliable treatment route for solid tumors (Sritharan and Sivalingam 2021). However, its usage is restricted due to heart tissue toxicity (Sharifi et al. 2020), and drug resistance to DOX remains inevitable (Ye et al. 2024). Therefore, extensive research is required to reduce DOX toxicity in non-target tissues while maintaining high efficacy in tumor tissues. Numerous studies demonstrate that nanozymes with DOX effectively inhibit the growth of breast cancer cells (Ning et al. 2021; Fan et al. 2021; Cheng et al. 2019).

The screening of anticancer drugs has traditionally been carried out using two-dimensional cell cultures due to their cost-effectiveness, speed, and multiple assays (Mó et al. 2020). However, two-dimensional cultures do not accurately represent cell–cell and cell–extracellular matrix (ECM) interactions (Carvalho et al. 2015). As a result, drug functions in this system can lead to false predictions of tumor response and clinical failures. Thus, it is noted that only around 5% of anticancer compounds advance to the clinical phase because of inadequate pharmacokinetics or uncertain efficacy (Wilhelm et al. 2016). Meanwhile, some argue that nanotechnology is on an uncertain path, relying on animal models without a full understanding of the intricate interactions of drug-resistant cancer cells events and the various biological barriers in human tissues (Sharifi et al. 2022). To address this challenge, three-dimensional cell culture from human cancer cells, known as spheroid models, have been recommended to better mimic the uniform tissue of cancer cells (Carvalho et al. 2015; Chen et al. 2022b). Despite limitations such as lack of interaction with the extracellular environment, lower physical resistance, and insufficient cell diversity, studies have shown that therapeutic responses in this model closely resemble in vivo conditions (Zhang et al. 2021; Cheng et al. 2019; Mó et al. 2020; Al-Kattan et al. 2020). In different scenarios, it has been revealed that the lack of complete penetration of therapeutic compounds due to high cell density and the presence of ECM, the change of oxygen gradient from the surface to the center, and the over-expression of anti-apoptotic proteins in the center of spheroids, anti-tumor therapeutic

responses are significantly different compared to two-dimensional cultures (Zhang et al. 2021; Reynolds et al. 2017; Law et al. 2020; Emami et al. 2021).

In this research, we developed Fe_3O_4/MnO_2@DOX hybrid nanozymes (FMDHN) with dual functionality for drug delivery and catalytic activity to inhibit MCF-7 cells. We then explored their anti-tumor effects in two-dimensional and spheroid models. Alongside analyzing the FMDHN' physicochemical characteristics and DOX loading/release capabilities, we investigated the enhanced efficacy against MCF-7 cells through synergistic actions with PTT. Our findings suggest that using FMDHN with catalytic properties and targeted drug release can create a new therapeutic opportunity for treating drug-resistant cells. However, focusing on cell organizational structures is crucial for advancing therapeutic objectives.

Material and methods

Materials

All chemical and biological materials utilized in this research were procured from Merck, Germany. Human breast cancer MCF-7 cells were acquired from Shahroud University of Medical Sciences.

Synthesis of FMDHN

The Fe_3O_4 nanozymes were synthesized using the solvothermal approach. Iron (III) chloride (3.25 g) and tri-sodium citrate (1.3 g) were dispersed in 100 mL of ethylene glycol and stirred continuously for 30 min. Subsequently, sodium acetate (6.0 g) was added to the mixture and sonicated for 1 h. The resulting solution was then transferred to an autoclave set at 220 °C and left for 10 h. Following cooling, the product was washed three times with ethanol and distilled water before being dispersed in deionized water. Next, poly (acrylic acid) (PAA) (20 mg, 0.2 g/mL) and 150 µL of NH_4OH (5 M) were added to the Fe_3O_4 solution. The mixture was stirred for 20 min. Subsequently, 80 mL of isopropanol was gradually introduced to the solution with vigorous shaking to produce Fe_3O_4@PAA. Following this, 100 µL of Mn (II) acetate tetrahydrate (50 mg/mL) was carefully dripped into the solution and stirred for 3 h. The resulting Fe_3O_4/MnO_2 hybrid nanozymes (FMHN) were separated by centrifugation and washed with deionized water. The resulting precipitate was dried at 60 °C, and the FMHNs were then calcined at 450 °C in an N_2 atmosphere for 4 h. To load DOX (doxorubicin), 10 mg of FMHNs were added to 25 mL of dimethyl sulfoxide solution with 9 mg of DOX and kept for 24 h with gentle agitation. The FMDHN were subsequently air-dried for 24 h at room temperature and washed with PBS for further use.

Characterization of FMDHN

To analyze the surface morphology and internal structures, field-emission scanning electron microscopy (FESEM; MIRA3, TESCAN) and high-resolution transmission electron microscopy (TEM; HRTEM, JEM-2010) were utilized with an acceleration voltage of 200 kV. The Zetasizer system (Malvern Instruments, UK) was employed to determine hydrodynamic size and zeta potential at 25 °C. N_2 absorption isotherms of the samples at liquid nitrogen temperature (-196 °C) were measured using Nova's Quantachrome automatic gas absorption system to assess the nanozyme cavities. The pore size distribution

was considered from the desorption branch of the isotherm through the Barth–Joyner–Holland process. X-ray diffraction patterns of nanozymes were obtained through the XRD method. X-ray examination was conducted with a D/max- using Cu Kα radiation (Rigaku, Japan) in continuous scan mode ranging from 20° to 70° with a step size of 0.02° and speed of 2°/min. Energy dispersive X-ray spectroscopy (EDS) and elemental mapping studies were carried out on a JEOL JEM2010 electron microscope at 100 kV. Also, the peroxidase-like activity of nanozymes were assessed (an UV–vis spectrometer, Shimadzu UV-2600) by studying the oxidation of TMB (3,3′,5,5′-tetramethylbenzidine) as a reaction substrate. To do this, 2 µL of 100 µg/mL Fe_3O_4 nanozymes, FMHN, and FMDHN without and with PTT (808 nm laser light: 2 W/cm^2 for 3 min) were mixed with 500 µL of sodium acetate buffer at pH 6.5, along with 2 µL of 20 mg/mL TMB and 2 µL of 30% H_2O_2. Subsequently, the solutions were incubated in darkness for 10 min to carry out the peroxidase-like activity. Furthermore, the rise in ambient temperature due to the use of PTT (808 nm laser light: 2 W/cm^2 for 3 min) on FMHN (5 mg/mL in water distiller) were monitored with a thermometer while being exposed to 808 nm wavelength irradiation at various intervals: 0, 5, 10, 20, 40, 80, 160, 320, and 640 s.

Loading and validation tests, and drug release study

To determine the loading capacity, 100 µg of FMHN was placed in drug solution with concentrations of 30, 60, 90, 120 and 150 µg for 24 h at room temperature with gentle shaking (at 100 rpm). After separation of FMDHN by magnet and washing by PBS, the remaining solution was assessed and analyzed (based on Eq. 1) by fluorescence spectroscopy as the initial solution (Hitachi F 2500 spectrometer).

$$\begin{aligned}\text{Loading efficiency (\%)} &= [(\text{DIS} - \text{DRS})/\text{DRS}] \times 100;\\ &\quad \text{DIS is the total amount ofDO}\\ &\quad \times \text{ in initial solution and DRS is the amount of DO}\\ &\quad \times \text{ remaining in the solution.}\end{aligned} \tag{1}$$

To explore drug loading, thermogravimetric analysis (TGA) was assessed using Perkin-Elmer TGA-7 under N_2 at a heating rate of 5 °C/min in the range of 70–450 °C. A superconducting quantum interference device (SQUID, MPMS-XL) was used to assess the magnetic properties of FMDHN, ranging from − 8000 to + 8000 G at 298 m. In the following, in vitro DOX release from FMDHN were conducted at 37 °C in a shaker at 150 rpm in PBS solution with pH of 7.2 and pH of 6.5 with and without PTT (808 nm laser irradiation: 2 W/cm^2 for 3 min). At specified time intervals (0.37, 0.75, 1.5, 3, 6, 12 and 24 h), 2 mL of the sample was withdrawn from each container and replaced with an equal volume of PBS to maintain a constant volume. The drug release extent was assessed by measuring the absorbance at 428 nm using a UV–vis spectrophotometer. The total DOX release was calculated using the following Eq. (2):

$$\begin{aligned}\textit{Cumulative DOX release}\ (\%) &= \frac{5 \times \sum_{i-1}^{n-1} c_i + 50 \times c_n}{\textit{weight of DOX on FMDHN}} \times 100;\\ &\quad C_i \textit{ and } C_n \textit{ denote the DOX}\\ &\quad \textit{concentrations at times i and n, respectively}\end{aligned} \tag{2}$$

O_2 and ·OH generation

O_2 generation in aqueous solutions was assessed using a portable dissolved oxygen meter (Seven2GO pro S9 DO, Mettler Toledo). To conduct the experiment, 100 µg/mL of Fe_3O_4 nanozymes, FMHN, FMDHN with and without PTT (808 nm laser irradiation: 2 W/cm^2 for 3 min) were introduced into 10 mL of sodium acetate buffer with 200 µL of 30% H_2O_2. The O_2 production (mg/mL) was measured at various intervals: 0, 18, 37, 75, 150, 225, 300, 450, and 600 s. Also, terephthalic acid was utilized to measure the ·OH level. Following the interaction of terephthalic acid with Fe_3O_4 nanozymes, FMHN, FMDHN with and without PTT (808 nm laser irradiation: 2 W/cm^2 for 3 min), and its conversion to 2-hydroxy terephthalic acid, the ·OH level was assessed at a wavelength of 430–435 nm.

Cell culture

The NIH3T3 and MCF-7 cells were cultured in Dulbecco's modified Eagle's medium (DMEM) (GIBCO, New York) with 10% fetal bovine serum (FBS, AusGeneX) and 1% penicillin/streptomycin. Cell flasks were maintained in an incubator at 37 °C with 5% CO_2 and 95% humidity. For cell transfer to new culture medium, trypsinization (0.25% trypsin–EDTA) and re-suspension in DMEM medium were performed.

Toxicity evaluation

Cytotoxicity tests were conducted using the MTT method on NIH3T3 and MCF-7 cells. Initially, a density of 8×10^3 NIH3T3 and MCF-7 cells were plated in a 96-well plate and incubated for 12 h at 37 °C in 5% CO_2. Subsequently, NIH3T3 cells were exposed to specific concentrations of 0.27, 0.54, 1.08, 2.16, 4.32, and 8.65 µg/mL of FMHN. Also, MCF-7 cells were exposed to various concentrations of DOX (0.31, 0.62, 1.25, 2.5, 5, and 10 µM), FMHN (0.27, 0.54, 1.08, 2.16, 4.32, and 8.65 µg/mL), and FMDHN (0.27, 0.54, 1.08, 2.16, 4.32, and 8.65 µg/mL). Additionally, a set of MCF-7 cells received treatment with an 808-nm laser at 2 W/cm^2 for 3 min following an 8-h exposure to FMDHN (0.27, 0.54, 1.08, 2.16, 4.32, and 8.65 µg/mL). Then, the cells were then incubated for 48 h. Afterward, they were rinsed and 100 µL of fresh medium containing 20 µL of MTT solution (3-(4,5-dimethyl-2-thiazolyl)-2,5-diphenyl-2H-tetrazolium bromide: 0.5 mg/mL) was introduced into each well. The culture medium was once again incubated in darkness at 37 °C for 4 h. The resultant purple formazan crystals were dissolved in 100 µL of DMSO (dimethyl sulfoxide), and the absorbance was assessed at 570 nm with a multi-well plate reader. The survival rates of treated and control cells were calculated using Eq. 3.

$$\begin{aligned}\text{Cell viability (\%)} = [&[\text{Optical density of dosing cells} - \text{Optical density of blank}] \\ &\div [\text{Optical density of control} - \text{Optical density of blank}]] \times 100\end{aligned} \tag{3}$$

Apoptosis and ROS assays

To further study the inhibition of MCF-7 cell growth by FMHN and DOX, the apoptosis level was assessed using the Annexin-V/PI Apoptosis Analysis Kit (Yeasen, Inc., China) and flow cytometry. MCF-7 cells were seeded in a 6-well plate at a density of 5×10^5 as described in "Cell culture" Section. And then incubated for 12 h. Afterward, the old culture medium was replaced with a new one containing DOX (2.5 µM), FMHN (2.16 µg/mL), and FMDHN (2.16 µg/mL) with and without PTT (808 nm laser irradiation, 2 W/

cm^2 for 3 min) onto the plates. The MCF-7 cells were then cultured at 37 °C with 5% CO_2 for 48 h. After incubation, MCF-7 cells were harvested by centrifugation at 1000 g (5 min) and washed thrice in cold PBS. The cells were trypsinized, resuspended in 200 µL of binding buffer, and then stained with Annexin V-FITC/Alexa Fluor 488 (5 µL) and propidium iodide (PI: 10 µL) following the manufacturer's instructions. Subsequently, the stained cells were analyzed using flow cytometry in the absence of light.

To assess intracellular ROS levels, 5×10^5 cells per well were seeded in a 6-well plate. After 12 h of incubation at 37 °C with 5% CO_2, the cells were treated with DOX (2.5 Mm), FMHN (2.16 µg/mL), FMDHN (2.16 µg/mL) without or with PTT (808 nm laser irradiation, 2 W/cm^2 for 3 min). The MCF-7 cells were re-incubated for 48 h. Subsequently, the cells were rinsed with PBS and treated with 10 µM 2,7-dichlorodihydrofluorescein. After a 30-min incubation period, the cells underwent two PBS washes. The level of ROS was then assessed using FACscan (BD Bioscience, USA) by measuring the fluorescence intensity of 2,7-dichlorofluorescein produced through the oxidation of 2,7-dichlorodihydrofluorescein.

MCF-7 spheroids formation, cytotoxicity and morphometry

To generate MCF-7 3D spheroids, a method involving reducing FBS levels on non-adherent surfaces was employed. Briefly, MCF-7 cells were cultured at a density of 10^3 cells in ultra-low-attachment 24-well plates with DMEM medium supplemented with high glucose, 0.5% FBS, and 2% penicillin–streptomycin (all sourced from Gibco, USA) at 37 °C in a 5% CO_2. The MCF-7 spheroids were then incubated for six days. Afterwards, the MCF-7 spheroids were exposed to varying concentrations of DOX (0.31, 0.62, 1.25, 2.5, 5, and 10 µM), FMHN (0.27, 0.54, 1.08, 2.16, 4.32, and 8.65 µg/mL), and FMDHN (0.27, 0.54, 1.08, 2.16, 4.32, and 8.65 µg/mL) for 48 h. Moreover, a set of MCF-7 spheroids received treatment with an 808-nm laser irradiation at 2 W/cm^2 for 3 min following an 8-h exposure to FMDHN (0.27, 0.54, 1.08, 2.16, 4.32, and 8.65 µg/mL). Proliferation and viability of MCF-7 spheroids were evaluated 48 h post-treatment with therapeutic compounds utilizing Alamar Blue cell viability reagent. As per the manufacturer's instructions, 10 µg/mL (one-tenth of the total culture medium volume) of Alamar Blue was added to each MCF-7 spheroid and kept to incubator for 24 h. Subsequent to the incubation period, fluorescence intensity was measured on plates at 535 nm excitation and 595 nm emission using a DTX 880 microplate reader from Beckman Coulter in Brea, CA. Furthermore, to study the growth inhibition of MCF-7 spheroids by DOX (1.25 and 5 µM), FMHN (1.08 and 4.32 µg/mL), FMDHN (1.08 and 4.32 µg/mL) without or with PTT (an 808-nm laser irradiation at 2 W/cm^2 for 3 min), the dimensions of spheroids were evaluated using images with ImageJ software on the 6th day (equivalent to the first day of treatment) and the 11th day (5 days after treatment).

Mechanisms of cytotoxicity

Total RNA extraction was performed using the Trizol reagent (Sinaclon Bio Science, Iran) on spheroids 5-day post-treatment. The concentration and purity of RNA samples were assessed using a Nanodrop spectrophotometer (Thermo Fisher Scientific, USA). DNase I was utilized to eliminate genomic contamination from the isolated RNA.

Table 1 Primer sequence

Gene	Forward primer	Reverse primer
TNF-α	5′-CTCTTCTGCCTGCTGCACTTTG-3′	5′-ATGGGCTACAGGCTTGTCACTC-3′
CASP7	5′-CGGAACAGACAAAGATGCCGAG-3′	5′-AGGCGGCATTTGTATGGTCCTC-3′
Bcl-2	5′-ATCGCCCTGTGGATGACTGAGT-3′	5′-GCCAGGAGAAATCAAACAGAGGC-3′
CASP9	5′-GTTTGAGGACCTTCGACCAGCT-3′	5′-CAACGTACCAGGAGCCACTCTT-3′
CASP3	5′-GGAAGCGAATCAATGGACTCTGG-3′	5′-GCATCGACATCTGTACCAGACC-3′
β- actin	5′-CTTCTACAATGAGCTGCGTG-3′	5′-TCATGAGGTAGTCAGTCAGG-3′

Complementary DNA (cDNA) was generated using the BONmiR™ qRT-PCR miRNA Detection Kit (Stem Cell Technology Research Center, Tehran, Iran) following the manufacturer's instructions. Quantitative real-time PCR was conducted using SYBR Premix Ex Taq™ II (Takara Bio, Japan) and monitored with the Applied Biosystems® StepOneTM instrument and ABI7500 thermocycler following this protocol: initial activation at 95 °C for 5 min, 40 cycles of denaturation at 95 °C for 5 s, and annealing/extension at 60 °C for 30 s. The primer sequences are listed in Table 1. β-Actin served as the internal reference gene for normalizing gene expression. mRNA expression level was determined using the $2^{-(\Delta\Delta CT)}$ method. All reactions were conducted in triplicate.

Statistical analysis

The data were analyzed using one-way analysis of variance. Statistical significances were assessed with the Statistical Package for Social Science (version 20) and Tukey's multiple comparison tests. P-values below 5% were deemed statistically significant.

Results

Morphology and chemical properties

The morphology and size features of the engineered hybrid nanozymes, as revealed by SEM (Fig. 1A and B) and TEM (Fig. 1C) analyses, indicate that the FMDHN, ranging from 150 to 270 nm, consist of two fused nanospheres with surface cavities. While the DLS results indicate that the size of FMDHN ranges vary from 90 to 370 nm, the highest concentration can be seen in the range of 140–270 nm (Fig. 1D). Meanwhile, the porous structure of the FMHN was verified through nitrogen absorption and desorption output, as depicted in Fig. 1E. The N_2 adsorption–desorption isotherm outcomes exhibit type IV behavior with noticeable residual rings within the 0.30–0.44, 0.45–0.78 and 0.79–0.97 P/P0 range. The surface area of the FMHN was calculated at 65.266 m^2/g, featuring cavities ranging from 1.2 to 34.7 nm with an average size of 7.34 nm (Fig. 1F). Moreover, the zeta potential measurements reveal that Fe_3O_4 nanozymes and FMHN exhibit -3.14 mV and -25.2 mV values, respectively, under neutral conditions, demonstrating the effective incorporation of MnO_2 into the Fe_3O_4 nanozymes (Fig. 1G). Also, Fig. 1H illustrates the XRD patterns of Fe_3O_4 nanozymes and FMHN. The Fe_3O_4 nanozymes (black curve) shows diffraction peaks at ($2\theta = 30.1°$: 220), ($2\theta = 35.0°$: 311), ($2\theta = 44.6°$: 400), ($2\theta = 54.6°$: 422), ($2\theta = 56.6°$: 511), and ($2\theta = 63.5°$: 440) corresponding to Fe_3O_4 (PDF#19-629). In contrast, the hybrid nanozymes (red curve) exhibits these Fe_3O_4 peaks along with two additional peaks at $2\theta = 27.3°$ and $2\theta = 36.9°$, indicating the

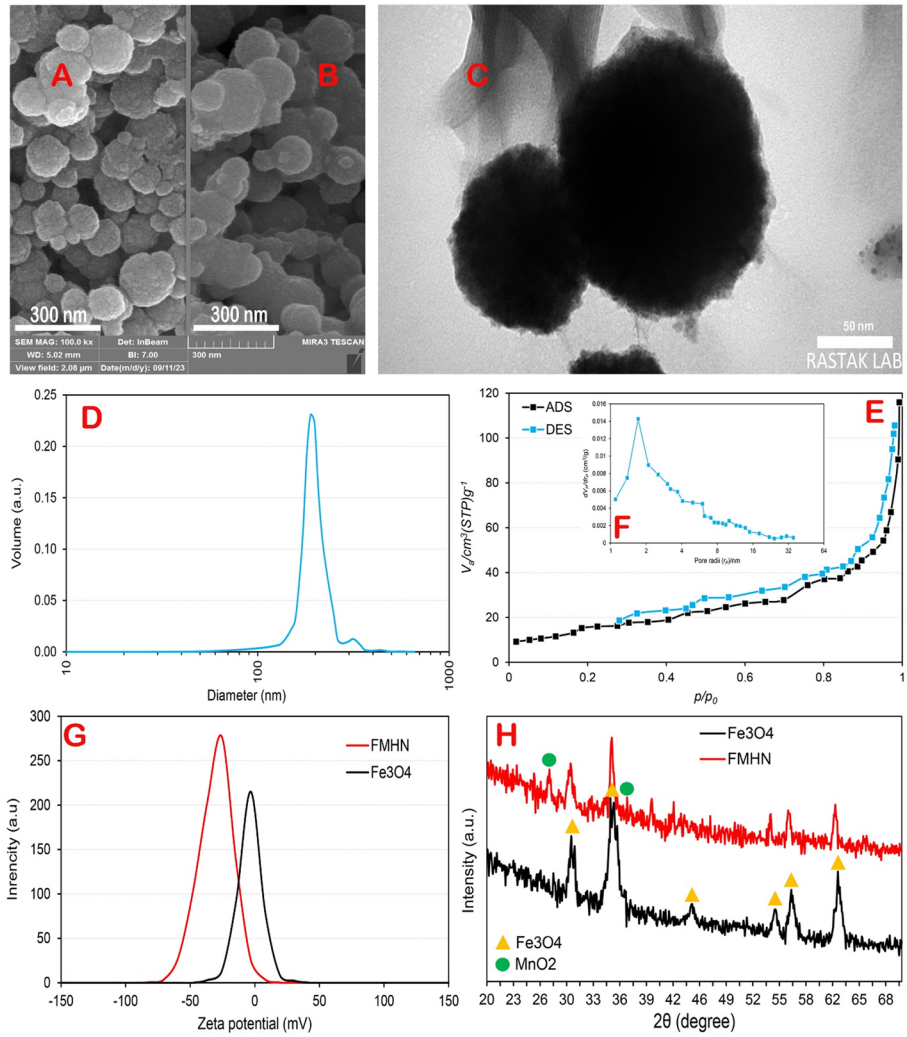

Fig. 1 Characterizations of the FMDHN. **A** SEM images of FMHN and **B** FMDHN. **C** TEM images of FMDHN. **D** the size distribution and **E** N_2 adsorption–desorption isotherms [**F** The size of pores on FMHN is indicated by the inset] of FMHN. **G** Zeta potential values of Fe_3O_4 nanozymes and FMHN. **H** XRD patterns of the synthesized Fe_3O_4 nanozymes and FMHN

presence of MnO_2 nanozymes (PDF#30-0820). This suggests that Mn(II) acetate was calcined to produce Fe_3O_4/MnO_2. In the following, elemental mapping from EDS analysis reveals the atomic distribution of metal ions on FMHN (Fig. 2A and B) with an Mn:Fe:O weight ratio of 37.3%: 22.6%: 40.1%. The mapping indicates that Fe is concentrated in the smaller nanospheres while Mn is predominant in the larger one (Fig. 2C).

The Fig. 2D data indicate that exposing the nanozymes to 808 nm laser irradiation at 2 W/cm^2 for 3 min' results in a temperature rise across various pH levels. Transitioning from a neutral (pH 7.2) to an acidic (pH 6.5) environment, akin to the acidity found in cancerous tumors, effectively triggers heat generation from FMHN. Also, the investigating the peroxidase-like activity revealed that FMHN exhibit favorable peroxidase characteristics in the presence of H_2O_2 and at a pH of 6.5. In Fig. 2E, TMB is converted by nanozymes into the blue oxTMB product. As anticipated, the inclusion of MnO_2 on the

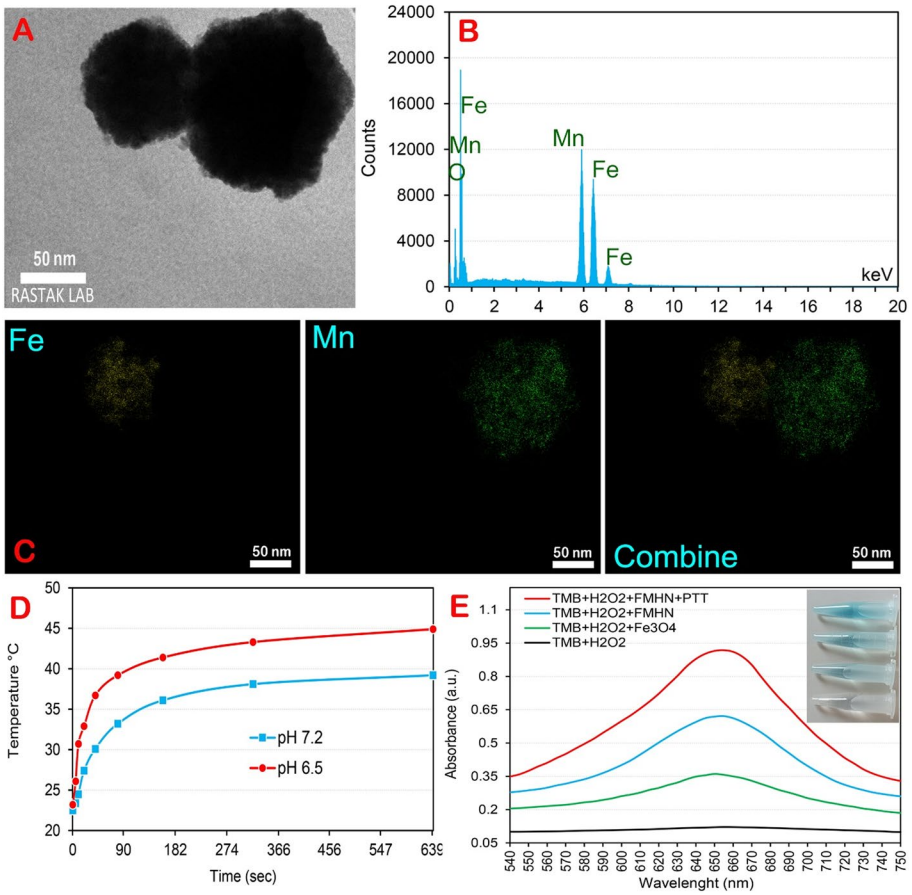

Fig. 2 **A** Representative TEM images of FMHN, **B** EDS and **C** element mapping of FMHN. **D** Temperature versus irradiation time of the FMHN suspensions with concentrations of 5 mg/mL in distilled water. **E** Peroxidase-like activities of Fe_3O_4 nanozymes, FMHN with and without PTT

Fe_3O_4 nanozymes enhances the catalytic performance. Furthermore, the synergism of PTT with FMHN significantly enhances the catalytic efficiency.

Loading and validation tests, and drug release

DOX loading content in Fig. 3A revealed that as the concentration of DOX increased, the rate of drug loading in FMHN also significantly increased with nanozymes constant concentration. However, as anticipated, the drug loading efficiency percentage decreased with higher DOX concentration. In summary, the findings indicate that the highest drug loading efficiency percentage (over 50%) is achieved with 30 and 60 µg of drug in 100 µg of FMHN. However, the concentration of 60 µg of DOX per 100 µg of FMHN was selected to ensure an effective therapeutic level of DOX by managing the dosage of FMHN in the body, achieving a loading efficiency of 51.3%. In this regard, TGA confirmed DOX presence in FMHN. As shown in Fig. 3B, FMHN exhibit high stability at temperatures up to 450 °C. The slight mass decrease of FMHN between 100 and 300 °C in the thermogram, accounting for ~ 4.9% by weight, is attributed to water loss within the pores and minor structural damage to FMHN. However, the

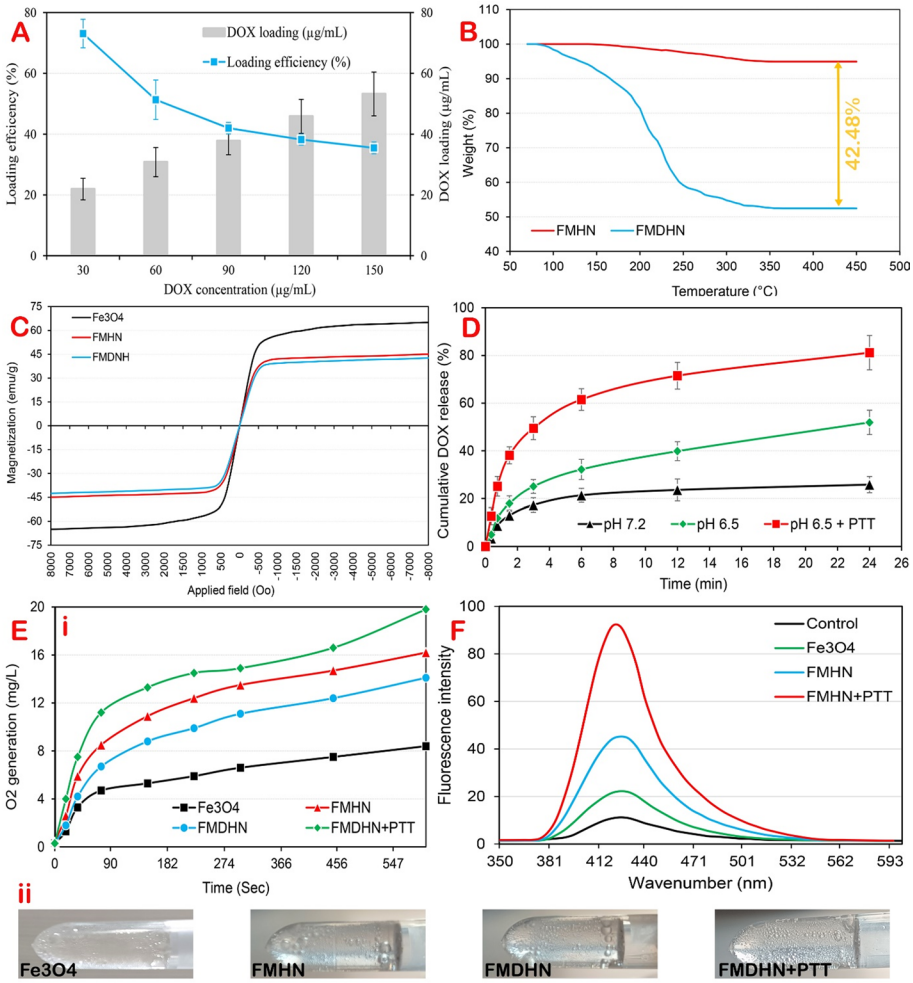

Fig. 3 **A** Drug loading and its efficiency. **B** Thermogravimetric analysis of FMHN and FMDHN, and their weight loss between 70 and 450 °C heating. **C** Magnetization curves at room temperature for Fe_3O_4 nanozymes, FMHN and FMDHN. **D** Quantitative analyses of DOX release at 37 °C at different pH with and without PTT. **E** O_2 generation in H_2O_2 solution with Fe_3O_4 nanozymes, FMHN and FMDHN with and without PTT. **F** Fluorescence spectra of terephthalic acid incubated with Fe_3O_4 nanozymes, FMHN, FMDHN with and without PTT in the hypoxic condition to show the presence of ·OH

stability of FMHN in terms of weight percentage between 300 °C and 450 °C demonstrates their robustness. Concurrently, the TGA curve reveals a weight loss of up to 42.48% for FMDHN, confirming the presence of DOX on FMHN. The weight percentage decrease in FMDHN exhibits a two-step transition: a gradual decline from 95 °C to 190 °C (14.9% weight reduction) followed by a steeper decrease from 195 °C to 260 °C (27.4% weight reduction). This behavior is likely attributed to the structural segments and functional groups of the drug molecule undergoing degradation. Furthermore, to support the aforementioned results, it was observed that the magnetic saturation of Fe_3O_4 nanozymes consistently reduces from 64.9 emu/g to 45.0 emu/g and 42.6 emu/g in the presence of MnO_2 nanozymes and DOX (Fig. 3C). Hence, the assertion regarding drug loading on FMHN is substantiated.

The FMDHN' capability to release DOX was studied at 37 °C under varying acidity levels. Figure 2D illustrates that DOX release from the FMDHN is time-dependent. Generally, DOX release is higher in acidic conditions (51.9%) compared to neutral conditions (25.8%). Moreover, the synergism of PTT with acidic environment boosts DOX release up to 81.19% by enhancing the peroxidase-like activities of the FMDHN. Furthermore, a higher burst release of DOX from FMDHN is observed at pH 6.5 (17.93%), exceeding the release at pH 7.2 (12.98%). Despite the somewhat negative impact of PTT in an acidic environment on the burst release of DOX, with an increase of up to 38.12%, controlled release improvement can help maintain a stable therapeutic dosage over 24 h. Furthermore, by enhancing FMDHN performance in acidic conditions, particularly through synergistic effects, it becomes feasible to boost DOX delivery in tumor areas with pH levels ranging from 6 to 6.5. This can also elevate drug efficacy by concentrating it in tumor tissues. Evidence for this was seen in the significant reduction of drug release at pH 7.2.

O_2 Generation

Evaluation of catalytic activity in Fig. 3E indicates that the presence of MnO_2 nanozymes on the Fe_3O_4 nanozymes enhances the nanozyme's catalytic activity for O_2 generation by nearly twofold, increasing from 8.4 to 16.2 mg/L. Despite the negative impact of DOX loading on the catalytic activity of FMHN in O_2 generation (14.1 mg/L), this study indicates that the combined effect of PTT with FMDHN notably enhances the catalytic activity for O_2 generation (19.8 mg/L) (Fig. 3E). Overall, this discovery indicates that boosting O_2 generation through FMHN post DOX release, or utilizing FMDHN alongside PTT (808 nm laser irradiation: 2 W/cm^2 for 3 min), can mitigate hypoxia and enhance drug permeation. In the following, the results depicted in Fig. 3F indicate that the FMHN effectively enhance the ·OH level compared to non-hybrid nanozymes. This enhancement is evidenced by the increased fluorescence intensity of 2-hydroxyterephthalic acid. While the presence of DOX on the FMHN decreases the ·OH level, it seems that the release of the drug at pH 6.5 leads to an increase in ·OH levels. Moreover, the study revealed that the FMDHN, in synergism with PTT, significantly elevate the ·OH level compared to other experimental groups.

Cytotoxicity of FMDHN

To investigate the toxicity effect of nanozymes with and without DOX loading, MTT and flow cytometry techniques were employed on NIH-3T3 cells and MCF-7 cells. Figure 4A shows that NIH-3T3 cells exhibited no significant cytotoxicity when treated with FMHN at concentrations of 0.27, 0.54, 1.08, and 2.16 μg/mL. However, toxicity increased when the concentration was raised to 4.32 μg/mL or higher. This study demonstrates that FMHN exhibit favorable biocompatibility as both a catalytic agent and a carrier for delivering anticancer drugs, particularly within a specific range. Similar to the toxicity output in NIH-3T3 cells, it was found in Fig. 4B that the toxicity of DOX, FMHN with and without DOX, combined with PTT (808 nm: 2 W/cm^2 for 3 min) on MCF-7 cells, is dose-dependent. The study indicates that the most significant suppression of MCF-7 cells by FMDHN occurs at doses of 2.16, 4.32, and 8.64 μg/mL compared to the control group (60.3%, 70.8% and 72.8% growth inhibition). However, based on the toxicity

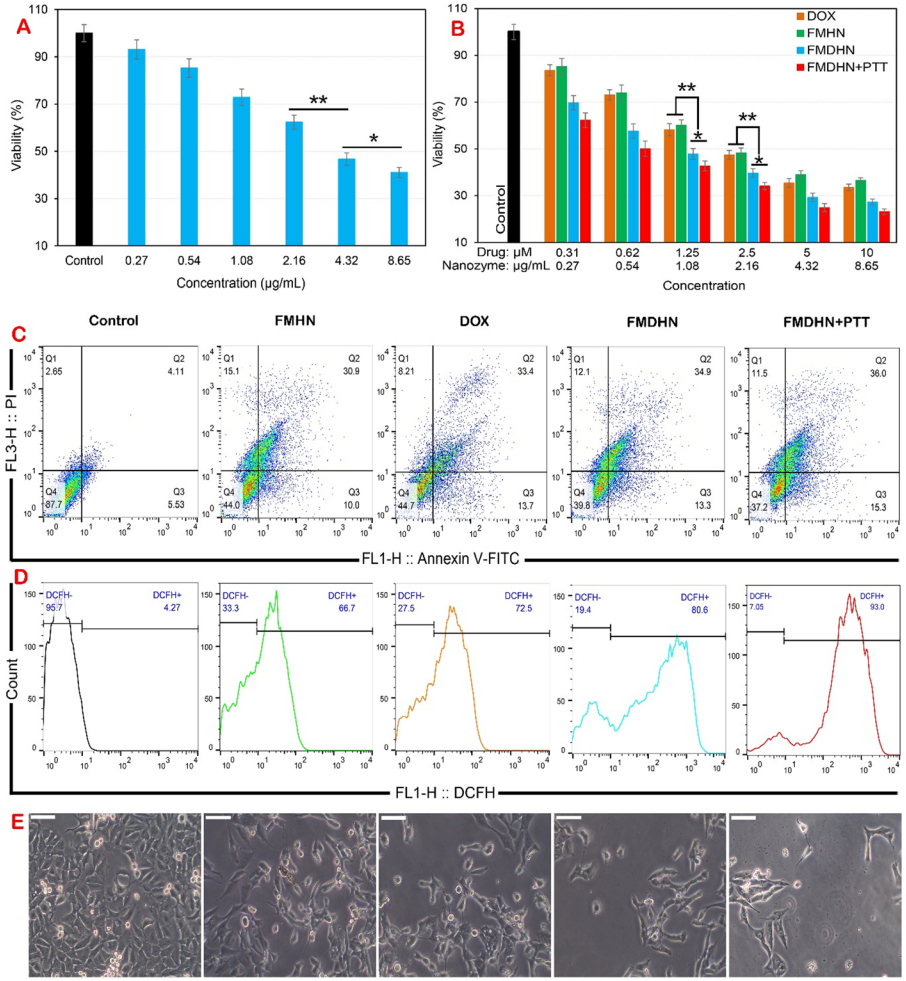

Fig. 4 **A** Cytotoxicity assay of FMHN on NIH-3T3 cells by MTT assay: $^{*}P < 0.05$, and $^{**}P < 0.01$. **B** MCF-7 cells viability after incubation with different concentrations of DOX, FMHN and FMDHN with and without PTT for 48 h. **C** Flow cytometric analysis of live and dead MCF-7 cells in different treatment groups: control, FMHN (2.16 μg/mL), DOX (2.16 μM), FMDHN (2.16 μg/mL) with and without PTT. Cell necrosis and apoptosis measured using propidium iodide (PI) and Annexin V-FITC staining. **D** Representative DCFH staining of MCF-7 cells in different treatments for ROS evaluation. **E** Optical microscopy images of MCF-7 cells treated with different treatments (scale bar: 100 μm)

dose of FMHN in Fig. 4A, it is recommended to use a dose of 2.16 μg/mL (equivalent to 2.5 μM DOX). In addition, it was discovered that the synergistic effect of FMDHN with PTT (808 nm: 2 W/cm^2 for 3 min) enhances the toxicity level of nanozymes on cancer cells from 2.16 μg/mL (65.9% growth inhibition) to 1.08 μg/mL (57.3% growth inhibition). It was also revealed that nanozymes, as nanocarriers, significantly increase the toxicity of DOX in all doses compared to DOX. Ultimately, the dose-dependent cytotoxicity of DOX in MCF-7 cells can be enhanced by two methods: loading on nanozymes and synergy with PTT, without inducing toxicity in non-cancerous cells.

After determining the toxicity dose from Fig. 4B, to analyze the percentage of apoptotic and necrotic cells during therapeutic activities, MCF-7 cells were exposed to 2.16 μg/mL concentrations of FMDHN with and without PTT, along with

2.5 μmol DOX. Flow cytometry results in Fig. 4C indicate that while DOX led to an increase in late and early apoptotic cells compared to the control (Q2: 33.4% vs 4.11%; Q3: 13.7% vs 5.53%), employing FMDHN as a drug carrier effectively raised late and early apoptotic cell levels by 34.9% and 13.3%, respectively. Also, it was found that the combination of PTT (808 nm: 2 W/cm^2 for 3 min) with FMDHN induced the highest levels of early (Q2: 36.0%) and late (Q3: 15.3%) apoptotic cells in MCF-7 cells. In support of the crucial role of apoptosis, Fig. 4D demonstrates that the FMHN and DOX significantly raised the intracellular ROS level compared to the control. Furthermore, loading DOX on FMHN resulted in a higher intracellular ROS level. Figure 4D illustrates that the greatest intracellular ROS is achieved through the synergy of FMDHN with PTT, confirming the heightened apoptotic level in this particular group. Thus, it was discovered that DOX, FMHN, FMDHN with and without PTT, induce the demise of MCF-7 cells by elevating intracellular ROS levels, leading to apoptosis. Supporting this conclusion, the morphological alterations (like changes in volume and shape) and the quantity of cancer cells exposed to DOX, FMHN, FMDHN with and without PTT, as depicted in Fig. 4E, indicate an anticipated cell demise.

Toxicity in MCF-7 spheroids

To investigate the impact of nanozymes toxicity on spheroids from MCF-7 cells, the MTT technique was employed. Figure 5A illustrates that DOX and FMHN exhibit dose-dependent toxicity, with no significant variance observed across different concentrations. The study found that the highest toxicity to MCF-7 spheroids occurred at 10 μM for DOX (59.75% growth inhibition) and at 8.64 μg/mL for FMHN (60.08% growth inhibition). Notably, the first observed toxic concentrations for DOX and FMHN were 5 μM (48.48% growth inhibition) and 4.32 μg/mL (49.32% growth inhibition), respectively. However, loading DOX onto FMHN enhances toxicity levels to 2.16 μg/mL (equivalent to 2.5 μM of DOX). Also, Fig. 5A clearly indicates that utilizing PTT (808 nm: 2 W/cm^2 for 3 min) in synergism with FMDHN exhibits superior anticancer effects across various concentrations. Although the synergistic group exhibits high toxicity at 4.32 μg/mL (72.8% growth inhibition) and 8.65 μg/mL (75.5% growth inhibition), significant toxicity is also noted at a concentration of 1.08 μg/mL FMDHN + PTT (55.1% growth inhibition).

After establishing the toxic dose of DOX, FMHN and FMDHN with or without PTT in MCF-7 spheroids (Fig. 5A), MCF-7 spheroids were treated with 1.25 and 5 μM DOX, 1.08 and 4.32 μg/mL FMHN, and 1.08 and 4.32 μg/mL FMDHN with and without PTT to assess the growth inhibition ratio. The criterion for assessing FMDHN concentration in both synergistic and non-synergistic activities is the observation of the initial toxic dose of FMHN and DOX in the presence of MCF-7 spheroids. In Fig. 5B rapid growth is observed in the spheroids of the control group, which are generally dense with a size of 168.3 ± 6.5 μm visible on the 5th day (103 ± 8.5 μm on the first day). The DOX (1.25 μM) and FMHN (1.08 μg/mL) groups effectively suppressed spheroid growth compared to the control group, showing no significant difference between them (Fig. 5B). At concentrations of 5 μM DOX (Fig. 5C(i)) and 4.32 μg/mL (Fig. 5C(i)) FMHN, the sizes were

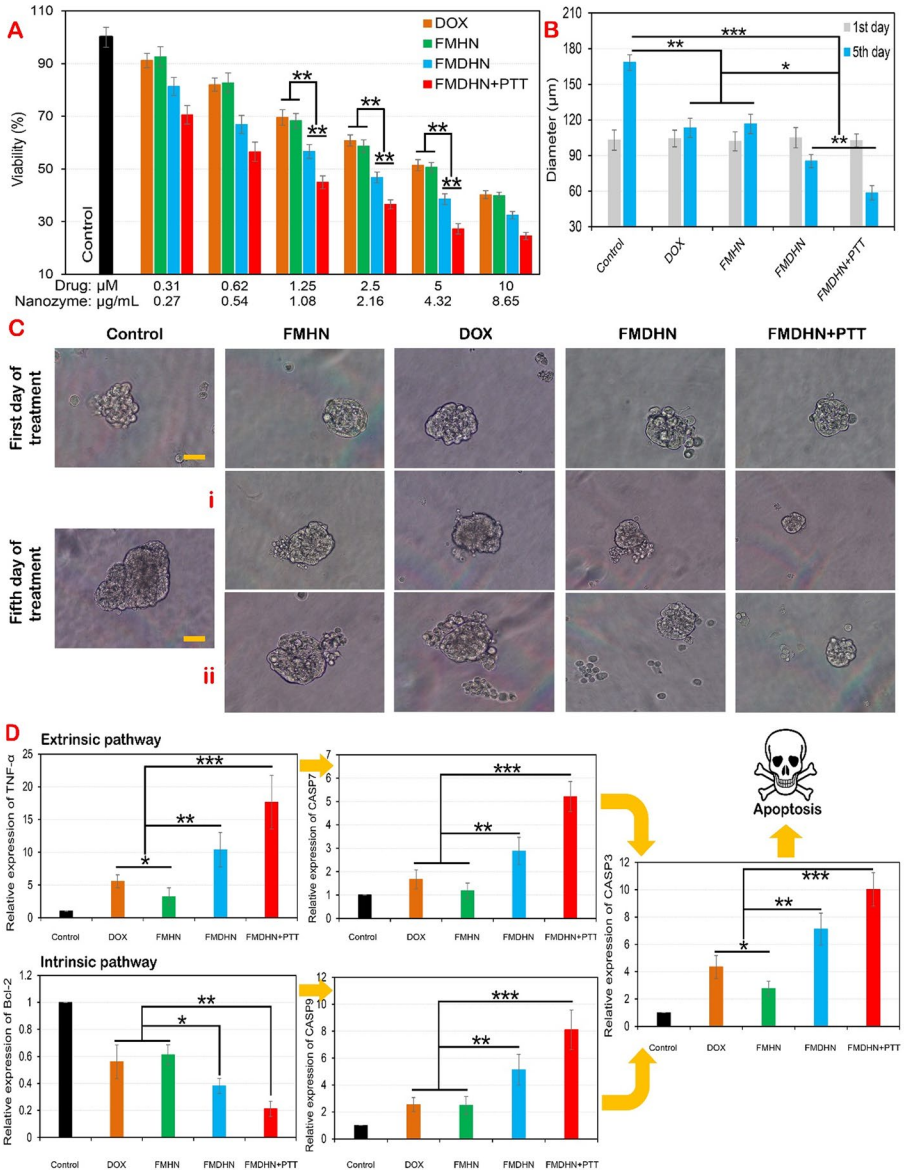

Fig. 5 **A** Viability of MCF-7 spheroids after incubation with different concentrations of DOX, FMHN and FMDHN with and without PTT for 48 h. **B** Average of diameter of MCF-7 spheroids in different treatment groups. **C** Images of MCF-7 spheroids incubated in different treatment groups: (i) control, FMHN (4.32 μg/mL), DOX (5 μM), FMDHN (4.32 μg/mL) with and without PTT (Scale bar: 50 μm), (ii) control, FMHN (1.08 μg/mL), DOX (1.25 μM), FMDHN (1.08 μg/mL) with and without PTT (Scale bar: 50 μm), **D** the effect of DOX, FMHN and FMDHN with and without PTT on the extrinsic and intrinsic mechanisms of apoptosis by examining the expression of TNF-α, CASP7, Bcl-2, CASP9, and CASP3 in MCF-7 spheroids. $^{*}P<0.05$, $^{**}P<0.01$ and $^{***}P<0.001$ indicate significant differences

113.3 ± 8 and 116.6 ± 8.1 μm, compared to 163 ± 6.5 μm in the control. Despite the significant inhibition of MCF-7 spheroid growth at above concentrations, DOX and FMHN levels were reduced to 1.25 μM and 1.08 μg/mL, respectively, to mitigate toxicity in normal cells (Fig. 5C(ii)). However, with MCF-7 spheroid sizes changing from 113.3 ± 8 to 132.1 ± 4 μm and 116.6 ± 8.1 to 134.3 ± 5, μm, respectively, the treatment process may be prolonged or ineffective (Fig. 5C(ii)). While the combination of DOX and FMHN

(FMDHN) significantly reduced MCF-7 spheroid growth compared to the control, decreasing the FMDHN dose from 4.32 μg/mL (Fig. 5C(i)) to 1.08 μg/mL (Fig. 5C(ii)) resulted in a relative decline in MCF-7 spheroids growth inhibition. Likewise, the combination of PTT with FMDHN significantly inhibited MCF-7 spheroids compared to the control at both 4.32 and 1.08 μg/mL concentrations, with sizes of 41.2 and 60.8 μm, respectively.

Cytotoxicity mechanisms

The toxicity mechanism depicted in Fig. 5D illustrates that FMDHN, with or without PTT, are highly effective in triggering apoptosis through intrinsic and extrinsic pathways. However, in terms of synergistic activity, the upregulation of TNF-α (17.64 vs. 10.38) and CASP7 (5.20 vs. 2.88) associated with the extrinsic pathway, along with the downregulation of Bcl-2 (0.21 vs. 0.38) and the elevation of CASP9 (8.10 vs. 5.12) compared to the FMDHN, offer greater promise in the treatment process. Despite the lack of significant differences between the DOX and FMHN groups in apoptosis pathways, DOX not only enhances apoptosis induction by increasing CASP3 (4.35 vs. 2.77), but also influences the extrinsic pathway by boosting TNF-α (5.55 vs. 3.20). In conclusion, these findings affirm that synergistic therapeutic approaches yield more dependable outcomes in cancer treatment.

Discussion

Nowadays, the use of nanozymes with varied catalytic capabilities controlled by pH and constituent elements, along with their integration with therapeutic techniques like PTT, has garnered significant interest. Nonetheless, beyond environmental obstacles and sustained catalytic performance (Khan et al. 2021), their efficacy within the therapeutic window dictated by the biological conditions of tumors or tumor cells poses a challenge. By enhancing controllable catalytic activity through element combinations and addressing environmental hurdles (Sharifi et al. 2023), it is hoped that tumor treatment procedures can be enhanced by enhancing drug penetration via reducing hypoxia levels, and modifying the tumor microenvironment (Wang et al. 2024a). With this premise, following the study of FMDHN and their structural and physicochemical analysis (Figs. 2 and 3), it was discovered that these nanozymes, with improved catalytic activity, lead to a greater O_2 and ·OH levels in hypoxic environments compared to non-hybrid nanozymes (Chen et al. 2023a; Wang et al. 2024b). According to the findings of Xu et al. (2022), it appears that increasing O_2 levels by enhancing drug permeability and increasing ·OH radical through inducing apoptosis can speed up the drug resistance cancer treatment process. This effect is particularly remarkable when combined synergistically with PTT and radiotherapy, as noted by Lv et al. (2021) and Li et al. (2019). Also, besides enhancing O_2 and ·OH levels, pH-responsive FMDHN offer a hopeful strategy for targeted drug delivery in drug-resistant cancers, ensuring efficient drug release at pH 6.5, particularly in synergistic actions, similar to the discoveries of Cheng et al. (2019), Meng et al. (2018), and Chen et al. (2023a). In line with findings of Wang et al. (Wang et al. 2024b) and Zhu et al. (2020), it was discovered that FMDHN, particularly in synergistic activity, demonstrates substantial toxicity against MCF-7 cells by promoting apoptosis through enhanced ROS. Nevertheless, in agreement with the findings of Nie et al. (2022) and Zeng et al. (2022),

it was found that the FMDHN, as opposed to DOX administration, could improve the treatment process by targeting of drug release, triggering intracellular ROS, and raising O_2 levels. This increase in the aforementioned events without synergistic effects by PTT could raise hopes for treating tumors inaccessible to laser irradiation. Despite the successes in limiting MCF-7 cell growth or removing them, the low efficacy of drugs or nanocarriers in clinical trials and human treatments has made researchers uncertain about their use. Although descriptive and analytical studies highlight the ineffectiveness of therapeutic approaches due to low EPR (enhanced permeability and retention), drug pump issues, high hypoxia from vessel blockage or excessive O_2 consumption, and physiological differences between animals and humans, and the cells derived from them (Sharifi et al. 2022), the analysis of therapeutic dosage based on the state of organization of cells in the early stages has received less attention. During this study, it was discovered that the optimal treatment dosage for MCF-7 spheroid structures under 200 μm differs significantly from that of two-dimensional cultures. The choice to select spheroids under 200 μm is based on the limitation of oxygen diffusion in tissues larger than 200 μm, as outlined in the empirical and mathematical modeling (Riffle and Hegde 2017). In the following, it was demonstrated that the optimal dosage of DOX and FMHN needs to be doubled when transitioning from two-dimensional culture to spheroids, going from 2.5 to 5 μM and from 2.16 to 4.32 μg/mL, respectively (Fig. 5A). While, the results in Fig. 4A indicate that raising the FMHN dosage to 4.32 μg/mL can lead to adverse effects on normal cells. On the other hand, it was revealed that the 2.16 μg/mL dose of FMDHN and its combination with PTT is still effective in reducing MCF-7 cell viability by 46.79% and 36.54%, respectively, even after the cells changed from a two-dimensional to a spherical. While, the negligible toxicity of FMHN in the FMDHN is maintained with 62.33% viability in NIH3T3 cells (Fig. 4A). Nevertheless, based on the effective dose of 1.08 μg of FMDHN with PTT on MCF-7 spheroids and a cell viability of 72.89% in NIH3T3 cells, this approach demonstrates significant value. Therefore, based on the findings of Al-Kattan et al. (2020), and Fig. 5A and C(ii), it is recommended to utilize synergistic activity with PTT to minimize the toxicity of FMDHN and enhance their effectiveness on cancerous tissues within the optimal concentration range for normal cells. In this regard, Fig. 5A and C(ii) illustrates that the synergy between FMDHN and PTT leads to a > 50% reduction in the survival of MCF-7 spheroids at a relatively safe dose of FMDHN (1.08 μg/mL) for normal cells. PTT synergy with FMDHN appears to effectively restrict spheroid growth through various actions, such as elevating O_2 and ·OH radical levels, enhancing drug release, and raising ambient temperature to 45 °C (Fig. 3F) to increase intrinsic and extrinsic apoptosis pathways (Fig. 5D). Furthermore, in line with the aforementioned discovery, Cheng et al. (2019), Zhang et al. (2021) and Emami et al. (2021) demonstrated that altering the organizational structure of MCF-7 and MCF-7/ADR, 4T1 and BT-20 cells from two-dimensional to spheroidal culture can impose less restrictions on the growth of drug-resistant cancer cells at the same dosage, due to decreased drug permeability. Confirming this discovery, it was found that as the dimensions of MCF-7 spheroids increase, the permeability of DOX and nanocarriers decreases (Holub et al. 2020). In this regard, Reynolds et al. (2017) demonstrated that while the growth of spheroids' periphery decreased, the core of spheroids significantly increased with the presence of cancer drugs. The limited drug access to the spheroids' core, attributed to

higher cell and collagen accumulation, appears to be the primary cause for reduced drug effectiveness. Based on finding of Brancato et al. (2018), it appears that the formation of ECM, caused by changing the culture medium from two-dimensional culture to spheroids, creates more complex barriers to drug penetration. Thus, it is anticipated that the dosage of therapeutic compounds will rise in spheroids as a result of altered drug/nanocarriers penetration patterns, potentially impacting their function through the presence of ECM.

Cellular organizations like spheroids versus two-dimensional cultures or larger spheroids versus small spheroids are more resistant to therapeutic activities due to reduced drugs/nanozymes penetration caused by a more compact ECM, changes in O_2 slope, and increased hypoxia in the center of the structure, as well as excessive expression of anti-apoptosis proteins (Bcl-2, BAX, etc.) in the center of cellular clusters (Reynolds et al. 2017; Riffle and Hegde 2017; Nunes et al. 2019). Therefore, it is recommended to use patterns closer to resistant tumors such as spheroids or organoids in academic/pharmaceutical centers to reduce the costs of the research-production process and explain the effects of drugs/nano-compounds.

Conclusions

In this study, following the creation and synthesis of FMDHN, we explored their combined performance with PTT. Physicochemical assessments verified the existence of iron and magnesium, showcasing their enzymatic functions in O_2 and ·OH production. The findings indicated that 150–270 nm-sized FMDHN could effectively partake in therapeutic tasks. These nanozymes exhibited thermal and biological stability at pH 7.2, featuring 7.34 nm pores, suggesting their potential as drug carriers in biological systems. Moreover, their capability to loading and release DOX reliably in an acidic environment (pH 6.5) similar to tumor tissues, particularly in the pH-responsive of FMDHN, enabled targeted drug delivery. In the following, the MTT and flow cytometry assessment indicates the high efficacy of FMDHN, particularly in synergy with PTT to inhibit cancer cell growth. However, toxicity evaluations of these nanozymes in MCF-7-derived spheroids demonstrate reduced toxicity levels at similar concentrations. While the synergistic effect is promising in limiting spheroid growth, escalating the FMDHN dose with associated side effects is deemed unacceptable. These findings underscore the importance of considering cellular organizational structures alongside the notable therapeutic responses of nanozymes.

Abbreviations

DLS	Dynamic light scattering
DMEM	Dulbecco's modified Eagle's medium
DOX	Doxorubicin
ECM	Extracellular matrix
EDS	Energy dispersive X-ray spectroscopy
FMDHN	Fe_3O_4/MnO_2@DOX hybrid nanozymes
FMHN	Fe_3O_4/MnO_2 hybrid nanozymes
MTT	3-(4,5-Dimethyl-2-thiazolyl)-2,5-diphenyl-2H-tetrazolium bromide
PBS	Phosphate-buffered saline
PCR	Polymerase chain reaction
PTT	Photothermal therapy
ROS	Reactive oxygen species
SEM	Scanning electron microscopy

TEM Transmission electron microscopy
TGA Thermogravimetric analysis
TMB Tetramethylbenzidine
XRD X-ray diffraction

Acknowledgements
The statements made herein are the sole responsibility of the authors.

Author contributions
MS, AAS, MM: conceptualization, methodology, revision; MS, MKF: analysis, validation, supervision; writing. All authors read and approved the final manuscript.

Funding
The present study was supported by Shahroud University of Medical Sciences, Shahroud, Iran, as a Ph.D. thesis (Grant Number: 200159). This research was carried out with the ethical code of IR.SHMU.AEC.1402.008.

Availability of data and materials
No datasets were generated or analysed during the current study.

Declarations

Consent for publication
All authors read and approve the final manuscript.

Competing interests
The authors declare no competing interests.

Received: 14 May 2024 Accepted: 18 September 2024
Published online: 28 September 2024

References

Al-Kattan A, Ali LMA, Daurat M, Mattana E, Gary-Bobo M (2020) Biological assessment of laser-synthesized silicon nanoparticles effect in two-photon photodynamic therapy on breast cancer MCF-7 cells. Nanomaterials 10:1462
Brancato V, Gioiella F, Imparato G, Guarnieri D, Urciuolo F, Netti PA (2018) 3D breast cancer microtissue reveals the role of tumor microenvironment on the transport and efficacy of free-doxorubicin in vitro. Acta Biomater 75:200–212
Carvalho MR, Lima D, Reis RL, Correlo VM, Oliveira JM (2015) Evaluating biomaterial-and microfluidic-based 3D tumor models. Trends Biotechnol 33:667–678
Chen M, Deng G, He Y, Li X, Liu W, Wang W, Zhou Z, Yang H, Yang S (2019) Ultrasound-enhanced generation of reactive oxygen species for MRI-guided tumor therapy by the Fe@ Fe3O4-based peroxidase-mimicking nanozyme. ACS Appl Bio Mater 3:639–647
Chen J, Chen T, Fang Q, Pan C, Akakuru OU, Ren W, Lin J, Sheng A, Ma X, Wu A (2022a) Gd2O3/b-TiO2 composite nanoprobes with ultra-high photoconversion efficiency for MR image-guided NIR-II photothermal therapy. Exploration 2:20220014
Chen G, Liu W, Yan B (2022b) Breast cancer MCF-7 cell spheroid culture for drug discovery and development. J Cancer Ther 13:117
Chen X, Tao H, Guo Y, Wang Z, Li R, Zhao Y, Liu C, Zhao X, Wang X, Duan S (2023a) Anti-CD44 antibodies grafted immunoaffinity Fe3O4@ MnO2 nanozymes with highly oxidase-like catalytic activity for specific detection of triple-negative breast cancer MDA-MB-231 cells. Anal Chim Acta 1249:340947
Chen K, Yan R, Yang H, Xia Y, Shang Y, Song J, Peng Z, Yang G (2023b) Multifunctional nanozymes by amplifying intracellular oxidative stress for enhanced photothermal-photodynamic therapy. ACS Appl Nano Mater 6:20855–20865
Cheng X, Li D, Sun M, He L, Zheng Y, Wang X, Tang R (2019) Co-delivery of DOX and PDTC by pH-sensitive nanoparticles to overcome multidrug resistance in breast cancer. Colloids Surf B 181:185–197
Cui M, Xu B, Wang L (2024) Recent advances in multi-metallic-based nanozymes for enhanced catalytic cancer therapy. Bmemat 2:e12043
Cun J-E, Pan Y, Zhang Z, Lu Y, Li J, Pan Q, Gao W, Luo K, He B, Pu Y (2022) Photo-enhanced upcycling H2O2 into hydroxyl radicals by IR780-embedded Fe3O4@ MIL-100 for intense nanocatalytic tumor therapy. Biomaterials 287:121687
de Melo-Diogo D, Pais-Silva C, Dias DR, Moreira AF, Correia IJ (2017) Strategies to improve cancer photothermal therapy mediated by nanomaterials. Adv Healthcare Mater 6:1700073
Dong H, Du W, Dong J, Che R, Kong F, Cheng W, Ma M, Gu N, Zhang Y (2022) Depletable peroxidase-like activity of Fe3O4 nanozymes accompanied with separate migration of electrons and iron ions. Nat Commun 13:5365
Du W, Chen W, Wang J, Zhang H, Song L, Hu Y, Ma X (2023) A dual-nanozyme-loaded black phosphorus multifunctional therapeutic platform for combined photothermal/photodynamic/starvation cancer therapy. J Mater Chem B 11:5185–5194
Emami F, Pathak S, Nguyen TT, Shrestha P, Maharjan S, Kim JO, Jeong J-H, Yook S (2021) Photoimmunotherapy with cetuximab-conjugated gold nanorods reduces drug resistance in triple negative breast cancer spheroids with enhanced infiltration of tumor-associated macrophages. J Control Release 329:645–664
Falahati M, Sharifi M, Hagen TLT (2022) Explaining chemical clues of metal organic framework-nanozyme nano-/micromotors in targeted treatment of cancers: benchmarks and challenges. Journal of Nanobiotechnology 20:153
Falahati M, Sharifi M, Vahdani Y, Haghighat S, ten Hagen TLM, Cai Y (2024) Catalytic imaging-guided cancer therapy using non-coordinated and coordinated nanozymes. Coord Chem Rev 507:215755

Fan S, Qi L, Li J, Pan D, Zhang Y, Li R, Zhang C, Wu D, Lau P, Hu Y (2021) Guiding the patterned growth of neuronal axons and dendrites using anisotropic micropillar scaffolds. Adv Healthcare Mater 10:2100094
Gao L, Zhuang J, Nie L, Zhang J, Zhang Y, Gu N, Wang T, Feng J, Yang D, Perrett S (2007) Intrinsic peroxidase-like activity of ferromagnetic nanoparticles. Nat Nanotechnol 2:577–583
Holub AR, Huo A, Patel K, Thakore V, Chhibber P, Erogbogbo F (2020) Assessing advantages and drawbacks of rapidly generated ultra-large 3D breast cancer spheroids: studies with chemotherapeutics and nanoparticles. Int J Mol Sci 21:4413
Khan S, Sharifi M, Bloukh SH, Edis Z, Siddique R, Falahati M (2021) In vivo guiding inorganic nanozymes for biosensing and therapeutic potential in cancer, inflammation and microbial infections. Talanta 224:121805
Law S, Leung AW, Xu C (2020) Folic acid-modified celastrol nanoparticles: synthesis, characterization, anticancer activity in 2D and 3D breast cancer models. Artif Cells Nanomed Biotechnol 48:542–559
Lei H, Pei Z, Jiang C, Cheng L (2023) Recent progress of metal-based nanomaterials with anti-tumor biological effects for enhanced cancer therapy. Exploration. https://doi.org/10.1002/EXP.20220001
Li Y, Yun K-H, Lee H, Goh S-H, Suh Y-G, Choi Y (2019) Porous platinum nanoparticles as a high-Z and oxygen generating nanozyme for enhanced radiotherapy in vivo. Biomaterials 197:12–19
Li J, Cai X, Zhang Y, Li K, Guan L, Li Y, Wang T, Sun T (2022) MnO2 nanozyme-loaded MXene for cancer synergistic photothermal-chemodynamic therapy. ChemistrySelect 7:e202201127
Liu S, Xu J, Xing Y, Yan T, Yu S, Sun H, Liu J (2022) Nanozymes as efficient tools for catalytic therapeutics. VIEW 3:20200147
Liu X, Sun T, Sun Y, Manshina A, Wang L (2024) Polyoxometalate-based peroxidase-like nanozymes. Nano Mater Sci. https://doi.org/10.1016/j.nanoms.2024.03.002
Lv W, Cao M, Liu J, Hei Y, Bai J (2021) Tumor microenvironment-responsive nanozymes achieve photothermal-enhanced multiple catalysis against tumor hypoxia. Acta Biomater 135:617–627
Meng L, Cheng Y, Tong X, Gan S, Ding Y, Zhang Y, Wang C, Xu L, Zhu Y, Wu J et al (2018) Tumor oxygenation and hypoxia inducible factor-1 functional inhibition via a reactive oxygen species responsive nanoplatform for enhancing radiation therapy and abscopal effects. ACS Nano 12:8308–8322
Mó I, Sabino IJ, Melo-Diogo Dd, Lima-Sousa R, Alves CG, Correia IJ (2020) The importance of spheroids in analyzing nanomedicine efficacy. Nanomedicine 15:1513–1525
Nie Z, Vahdani Y, Cho WC, Bloukh SH, Edis Z, Haghighat S, Falahati M, Kheradmandi R, Jaragh-Alhadad LA, Sharifi M (2022) 5-Fluorouracil-containing inorganic iron oxide/platinum nanozymes with dual drug delivery and enzyme-like activity for the treatment of breast cancer. Arab J Chem 15:103966
Ning S, Zheng Y, Qiao K, Li G, Bai Q, Xu S (2021) Laser-triggered combination therapy by iron sulfide-doxorubicin@ functionalized nanozymes for breast cancer therapy. J Nanobiotechnol 19:1–14
Nunes AS, Barros AS, Costa EC, Moreira AF, Correia IJ (2019) 3D tumor spheroids as in vitro models to mimic in vivo human solid tumors resistance to therapeutic drugs. Biotechnol Bioeng 116:206–226
Reynolds DS, Tevis KM, Blessing WA, Colson YL, Zaman MH, Grinstaff MW (2017) Breast cancer spheroids reveal a differential cancer stem cell response to chemotherapeutic treatment. Sci Rep 7:10382
Riffle S, Hegde RS (2017) Modeling tumor cell adaptations to hypoxia in multicellular tumor spheroids. J Exp Clin Cancer Res 36:1–10
Sharifi M, Jafari S, Hasan A, Paray BA, Gong G, Zheng Y, Falahati M (2020) Antimetastatic activity of lactoferrin-coated mesoporous maghemite nanoparticles in breast cancer enabled by combination therapy. ACS Biomater Sci Eng 6:3574–3584
Sharifi M, Cho WC, Ansariesfahani A, Tarharoudi R, Malekisarvar H, Sari S, Bloukh SH, Edis Z, Amin M, Gleghorn JP (2022) An updated review on EPR-based solid tumor targeting nanocarriers for cancer treatment. Cancers 14:2868
Sharifi M, Kheradmandi R, Alizadeh M (2023) Two birds with one stone: triple negative breast cancer therapy by PtCo bimetallic nanozyme coated with gemcitabine-hyaluronic acid-polyethylene glycol. Cancer Nanotechnol 14:41
Sisakhtnezhad S, Rahimi M, Mohammadi S (2023) Biomedical applications of MnO2 nanomaterials as nanozyme-based theranostics. Biomed Pharmacother 163:114833
Sohail M, Sun Z, Li Y, Gu X, Xu H (2021) Research progress in strategies to improve the efficacy and safety of doxorubicin for cancer chemotherapy. Expert Rev Anticancer Ther 21:1385–1398
Sritharan S, Sivalingam N (2021) A comprehensive review on time-tested anticancer drug doxorubicin. Life Sci 278:119527
Sun Y, Xu L, Liu X, Shen Y, Zhang Y, Gu N, Xiong F (2022) Coronal relay reactor Fe3O4@CeO2 for accelerating ROS axial conversion through enhanced Enzyme-like effect and relay effect. Chem Eng J 429:132303
Tang G, He J, Liu J, Yan X, Fan K (2021) Nanozyme for tumor therapy: surface modification matters. Exploration. https://doi.org/10.1002/EXP.20210005
Tang M, Zhang Z, Sun T, Li B, Wu Z (2022) Manganese-based nanozymes: preparation, catalytic mechanisms, and biomedical applications. Adv Healthcare Mater 11:2201733
Tang M, Ni J, Yue Z, Sun T, Chen C, Ma X, Wang L (2024) Polyoxometalate-nanozyme-integrated nanomotors (POMotors) for self-propulsion-promoted synergistic photothermal-catalytic tumor therapy. Angew Chem Int Ed 63:e202315031
Wang X, Teng Z, Wang H, Wang C, Liu Y, Tang Y, Wu J, Sun J, Wang H, Wang J (2014) Increasing the cytotoxicity of doxorubicin in breast cancer MCF-7 cells with multidrug resistance using a mesoporous silica nanoparticle drug delivery system. Int J Clin Exp Pathol 7:1337
Wang S, Cheng M, Wang S, Jiang W, Yang F, Shen X, Zhang L, Yan X, Jiang B, Fan K (2024a) A self-catalytic NO/O2 gas-releasing nanozyme for radiotherapy sensitization through vascular normalization and hypoxia relief. Adv Mater. https://doi.org/10.1002/adma.202403921
Wang X, Liu C, Chen X, Zhao X, Wu J, Chen H, Wan M, Zhao S, Li X, Li N, Duan S (2024b) A smart nitric oxide (NO) generating immuno-trimetallic nanocatalyst triggering chemodynamic therapy in breast cancer treatment. Adv Funct Mater. https://doi.org/10.1002/adfm.202316186
Wilhelm S, Tavares AJ, Dai Q, Ohta S, Audet J, Dvorak HF, Chan WC (2016) Analysis of nanoparticle delivery to tumours. Nat Rev Mater 1:1–12
Wu C-Y, Hsu Y-H, Chen Y, Yang L-C, Tseng S-C, Chen W-R, Huang C-C, Wan D (2021) Robust O2 supplementation from a trimetallic nanozyme-based self-sufficient complementary system synergistically enhances the starvation/photothermal therapy against hypoxic tumors. ACS Appl Mater Interfaces 13:38090–38104

Xu Q, Zhang Y, Yang Z, Jiang G, Lv M, Wang H, Liu C, Xie J, Wang C, Guo K (2022) Tumor microenvironment-activated single-atom platinum nanozyme with H2O2 self-supplement and O2-evolving for tumor-specific cascade catalysis chemodynamic and chemoradiotherapy. Theranostics 12:5155
Yang J, Zhang R, Zhao H, Qi H, Li J, Li J-F, Zhou X, Wang A, Fan K, Yan X, Zhang T (2022) Bioinspired copper single-atom nanozyme as a superoxide dismutase-like antioxidant for sepsis treatment. Exploration 2:20210267
Ye S, Chen S, Yang X, Lei X (2024) Drug resistance in breast cancer is based on the mechanism of exocrine non-coding RNA. Discover Oncol 15:138
Zeng Z, Wang Z, Chen S, Xiao C, Liu M, Zhang J, Fan J, Zhao Y, Liu B (2022) Bio-nanocomplexes with autonomous O2 generation efficiently inhibit triple negative breast cancer through enhanced chemo-PDT. J Nanobiotechnol 20:500
Zhang Y, Yang Y, Shi J, Wang L (2021) A multimodal strategy of Fe 3 O 4@ ZIF-8/GOx@ MnO 2 hybrid nanozyme via TME modulation for tumor therapy. Nanoscale 13:16571–16588
Zhang R, Jiang B, Fan K, Gao L, Yan X (2024) Designing nanozymes for in vivo applications. Nat Rev Bioeng. https://doi.org/10.1038/s44222-024-00205-1
Zhu X, Liu Y, Yuan G, Guo X, Cen J, Gong Y, Liu J, Gang Y (2020) In situ fabrication of MS@ MnO 2 hybrid as nanozymes for enhancing ROS-mediated breast cancer therapy. Nanoscale 12:22317–22329

Publisher's Note